A&A 462, 57–66 (2007)
DOI: 10.1051/0004-6361:20066277

Astronomy & Astrophysics

Hard X-ray luminosity function and absorption distribution of nearby AGN: INTEGRAL all-sky survey

S. Sazonov[1,2], M. Revnivtsev[1,2], R. Krivonos[2,1], E. Churazov[1,2], and R. Sunyaev[1,2]

[1] Max-Planck-Institut für Astrophysik, Karl-Schwarzschild-Str. 1, 85740 Garching bei München, Germany
e-mail: sazonov@mpa-garching.mpg.de
[2] Space Research Institute, Russian Academy of Sciences, Profsoyuznaya 84/32, 117997 Moscow, Russia

Received 20 August 2006 / Accepted 24 September 2006

ABSTRACT

Aims. We study the hard X-ray luminosity function and absorption distribution of local ($z \lesssim 0.1$) active galactic nuclei (AGN) and discuss the implications for AGN cosmological evolution and for the cosmic X-ray background (CXB).
Methods. We use the INTEGRAL all-sky hard X-ray survey to perform a statistical study of a representative sample of nearby AGN. Our entire all-sky sample consists of 127 AGN, of which 91 are confidently detected ($>5\sigma$) on the time-averaged map obtained with the IBIS/ISGRI instrument and 36 are detected only during single observations. Among the former there are 66 non-blazar AGN located at $|b| > 5^\circ$, where the survey's identification completeness is ∼93%, which we use for calculating the AGN luminosity function and X-ray absorption distribution.
Results. In broad agreement with previous studies, we find that the fraction f_a of obscured ($\log N_H > 22$) objects is much higher (∼70%) among the low-luminosity AGN ($L_{hx} < 10^{43.6}$ erg s^{-1}) than among the high-luminosity ones ($L_{hx} > 10^{43.6}$ erg s^{-1}), $f_a \sim 25\%$, where L_{hx} is the luminosity in the 17–60 keV energy band. We also find that locally the fraction of Compton-thick AGN is less than 20% unless there is a significant population of AGN that are so strongly obscured that their observed hard X-ray luminosities fall below $\sim 10^{40}$–10^{41} erg s^{-1}, the effective limit of our survey. The constructed hard X-ray luminosity function has a canonical, smoothly broken power-law shape in the range $40 < \log L_{hx} < 45.5$ with a characteristic luminosity of $\log L_* = 43.40 \pm 0.28$. The estimated local luminosity density due to AGN with $\log L_{hx} > 40$ is $(1.4 \pm 0.3) \times 10^{39}$ erg s^{-1} Mpc^{-3} (17–60 keV). We demonstrate that the spectral shape and amplitude of the CXB are consistent with the simple scenario in which the N_H distribution of AGN (for a given $L_{hx}/L_*(z)$ ratio) has not changed significantly since $z \sim 1.5$, while the AGN luminosity function has experienced pure luminosity evolution.

Key words. surveys – galaxies: active – galaxies: evolution – galaxies: Seyfert – X-rays: diffuse background

1. Introduction

Recent deep extragalactic X-ray surveys (see Brandt & Hasinger 2005, for a review) have significantly advanced our understanding of the cosmological evolution of active galactic nuclei (AGN) and the growth of massive black holes. In particular, these surveys have revealed the phenomenon of AGN "downsizing" , i.e. gradual transition from the dominance of luminous quasars at high redshift ($z \gtrsim 2$) to that of lower luminosity AGN at $z \lesssim 1$. Another important result is the discovery of numerous type 2 (i.e. with significant X-ray absorption) AGN at medium and high redshifts. Despite these successes, the census of AGN in the Universe may still be significantly incomplete, in particular because deep X-ray surveys, performed effectively at energies below ∼8 keV, are biased against detecting heavily obscured sources. Furthemore, since deep extragalactic X-ray surveys usually cover small areas on the sky, they do not probe the bright end of the AGN luminosity distribution at low redshift ($z \lesssim 0.3$). It is in these two overlapping areas – heavily obscured AGN and luminous nearby AGN – where deep X-ray surveys could be efficiently complemented by all-sky hard X-ray (above ∼10 keV) surveys.

Recently, a serendipitous all-sky survey in the 3–20 keV energy band was performed with the RXTE observatory (the RXTE Slew Survey, or XSS), in which ∼100 AGN were detected at $|b| > 10^\circ$ (Revnivtsev et al. 2004). This sample was used to construct an X-ray luminosity function of local ($z \lesssim 0.1$) AGN and to study their absorption distribution (Sazonov & Revnivtsev 2004). However, despite its harder X-ray range compared to traditional X-ray surveys, the XSS was still biased against finding sources with absorption columns $N_H \gtrsim 10^{23}$ cm^{-2}.

A comparable or better (for heavily obscured sources and/or in crowded sky regions) capability for studying bright ($\gtrsim$1 mCrab) hard X-ray sources is now provided by the IBIS telescope (Ubertini et al. 2003) of the INTEGRAL observatory (Winkler et al. 2003), owing to its good sensitivity above 20 keV, large field of view (∼28° × 28°), and good (∼10′) angular resolution. Since its launch in October 2002, INTEGRAL had observed ∼60% of the sky by the spring of 2005, mostly around the Galactic plane and the Galactic center. This motivated us to initiate a series of pointed INTEGRAL observations (Proposal 0320108) aimed at covering the remaining "empty" (extragalactic) sky regions. This campaign has now been completed and practically full coverage of the sky has been achieved after all public and our proprietary INTEGRAL observations were added.

Based on the all-sky hard X-ray map obtained and the follow-up source identifications, we compiled a catalog of detected sources (Krivonos et al. 2006). In the present paper we use the INTEGRAL all-sky survey to study such key statistical properties of the local AGN population as the hard X-ray

Table 1. INTEGRAL all-sky survey AGN sample.

Object (sources at $\|b\| < 5^\circ$ are given in bold)	Class[a]	z	D Mpc	Note[b]	$F_{17-60\,\mathrm{keV}}$ 10^{-11} erg/s/cm^2	$\log L_{\mathrm{hx}}$ erg/s	N_{H} 10^{22} cm^{-2}	Ref.[c]
AGN detected at $>5\sigma$ on the time-averaged IBIS/ISGRI map								
Mrk 348	S2	0.0150			7.41 ± 0.83	43.52	30	2
IGR J01528−0326 = MCG -01-05-047	S2	0.0172		1	1.63 ± 0.30	42.98		
NGC 788	S2	0.0136			4.83 ± 0.29	43.25	44	3
LEDA 138501	S1	0.0492			3.96 ± 0.72	44.30	<1	4
Mrk 1040	S1.5	0.0167			4.85 ± 0.81	43.43	<1	5
IGR J02343+3229 = NGC 973	S2	0.0162		1	3.88 ± 0.63	43.31		
NGC 1068	S2	0.0038	14.4		1.90 ± 0.30	41.68	$\gtrsim 10^3$	6
4U 0241+61	S1	0.0440			4.75 ± 0.60	44.28	<1	7
NGC 1142	S2	0.0288			4.61 ± 0.35	43.89	45	8
1H 0323+342	S1	0.0610			2.74 ± 0.47	44.34	<1	4
NGC 1365	S1.8	0.0055	16.9		3.30 ± 0.65	42.06	~50	9
3C 111	BLRG	0.0485			7.83 ± 0.87	44.59	<1	10
ESO 033-G002	S2	0.0181			1.94 ± 0.27	43.10	1	11
IRAS 05078+1626	S1.5	0.0179			5.93 ± 0.75	43.58	<1	4
Mrk 3	S2	0.0135			6.83 ± 0.30	43.39	110	6
Mrk 6	S1.5	0.0188			3.66 ± 0.30	43.41	~5	12
IGR J07563−4137 = 2MASX J07561963−4137420	S2	0.0210		2, 3	1.24 ± 0.24	43.04	<1	13
IGR J07597−3842	S1.2	0.0400		3	2.91 ± 0.26	43.98	<1	8
ESO 209-G012	S1.5	0.0405			1.66 ± 0.24	43.75	<1	4
Fairall 1146	S1.5	0.0316			1.62 ± 0.25	43.52	<1	4
IRAS 09149−6206	S1	0.0573			2.06 ± 0.26	44.16	<1	4
Mrk 110	NLS1	0.0353			5.86 ± 1.14	44.17	<1	3
IGR J09446−2636 = 6dF J0944370−263356	S1	0.1425		4	3.91 ± 0.74	45.27	<1	4
NGC 2992	S2	0.0077	30.5		5.08 ± 0.39	42.76	1	14
MCG -5-23-16	S2	0.0085			9.77 ± 0.84	43.14	2.3	15
NGC 3081	S2	0.0080	32.5		4.62 ± 0.56	42.77	50	14
ESO 263-G013	S2	0.0333			2.15 ± 0.39	43.69	40	16
NGC 3227	S1.5	0.0039	20.6		9.05 ± 0.84	42.67	<1	3
NGC 3281	S2	0.0107			3.87 ± 0.64	42.94	150	17
IGR J10386−4947 = 2MASX J10384520−4946531	S1	0.0600		5	1.47 ± 0.24	44.05	1	8
IGR J10404−4625 = LEDA 93974	S2	0.0239		6	2.11 ± 0.35	43.38	2.8	8
NGC 3783	S1	0.0097	38.5		12.28 ± 1.86	43.34	<1	3
IGR J12026−5349 = WKK 0560	S2	0.0280		2, 3	2.44 ± 0.30	43.59	2	13
NGC 4151	S1.5	0.0033	20.3		47.38 ± 0.43	43.37	8	15
Mrk 50	S1	0.0234			1.31 ± 0.23	43.16	<1	4
NGC 4388	S2	0.0084	16.8		17.89 ± 0.31	42.79	40	14
NGC 4395	S1.8	0.0011	3.6		1.55 ± 0.29	40.38	2	18
NGC 4507	S2	0.0118			10.93 ± 0.49	43.48	59	15
NGC 4593	S1	0.0090	39.5		5.86 ± 0.25	43.04	<1	3
NGC 4945	S2	0.0019	5.2		19.92 ± 0.36	41.81	220	6
ESO 323-G077	S1.2	0.0150			2.78 ± 0.35	43.09	30	8
IGR J13091+1137 = NGC 4992		0.0251		2	3.49 ± 0.41	43.65	90	13
IGR J13149+4422 = Mrk 248	S2	0.0366		7	2.16 ± 0.38	43.77		
Cen A	NLRG	0.0018	4.9		56.09 ± 0.32	42.21	11	15
MCG -6-30-15	S1.2	0.0077			3.62 ± 0.38	42.62	<1	5
Mrk 268	S2	0.0399			1.74 ± 0.30	43.76		
4U 1344−60	S1	0.0130		6	5.96 ± 0.25	43.30	<1	3
IC 4329A	S1.2	0.0160			16.15 ± 0.51	43.92	<1	5
Circinus galaxy	S2	0.0014	4.2		18.76 ± 0.26	41.60	400	6
NGC 5506	S1.9	0.0062	28.7		13.34 ± 0.66	43.12	2.6	15
IGR J14493−5534 = 2MASX J14491283−5536194				8	1.64 ± 0.23		10	8
IGR J14515−5542 = WKK 4374	S2	0.0180		3	1.55 ± 0.22	43.00	<1	8
IGR J14552−5133 = WKK 4438	NLS1	0.0160		3, 9	1.40 ± 0.23	42.85	<1	4
IC 4518	S2	0.0157			2.44 ± 0.23	43.08		
WKK 6092	S1	0.0156			1.66 ± 0.24	42.91	<1	19
IGR J16185−5928 = WKK 6471	NLS1	0.0350		3,9	1.73 ± 0.24	43.64		
ESO 137-G34	S2	0.0092			1.68 ± 0.23	42.45		
IGR J16482−3036 = 2MASX J16481523−3035037	S1	0.0313		6	2.61 ± 0.24	43.72	<1	8
NGC 6221	S2	0.0050	19.4		1.90 ± 0.28	41.94	1	20
IGR J16558−5203	S1.2	0.0540		3	2.93 ± 0.21	44.26	<1	8
NGC 6300	S2	0.0037	14.3		4.71 ± 0.45	42.07	25	15
IGR J17204−3554				10	1.13 ± 0.17		13	21
GRS 1734−292	S1	0.0214			7.42 ± 0.14	43.83	<1	22
IGR J17418−1212 = 2E 1739.1−1210	S1	0.0372		11	2.55 ± 0.29	43.86	<1	23
IGR J17488−3253	S1	0.0200		3	1.91 ± 0.14	43.19	<1	8
IGR J17513−2011	S1.9	0.0470		3	2.32 ± 0.17	44.03		
IGR J18027−1455	S1	0.0350		12	2.93 ± 0.22	43.87	<1	24
3C 390.3	BLRG	0.0561			6.16 ± 0.64	44.61	<1	3
IGR J18559+1535 = 2E 1853.7+1534	S1	0.0838		13, 14	2.27 ± 0.23	44.54	<1	23
1H 1934−063	S1	0.0106			1.77 ± 0.31	42.59	<1	4
NGC 6814	S1.5	0.0052	22.8		4.73 ± 0.41	42.47	<1	5
Cygnus A	NLRG	0.0561			5.77 ± 0.33	44.58	20	26
IGR J2018+4043 = 2MASX J20183871+4041003				15	1.89 ± 0.28		7	8
IGR J20286+2544 = MCG +04-48-002	S2	0.0142		16	3.31 ± 0.58	43.12	50	8
Mrk 509	S1.2	0.0344			5.51 ± 0.83	44.13	<1	15
IGR J21178+5139 = 2MASX J21175311+5139034				17	1.93 ± 0.34			
IGR J21247+5058	S1	0.0200		12	8.56 ± 0.34	43.84	<1	24
IGR J21277+5656	S1	0.0144		13	2.68 ± 0.45	43.04	<1	8
NGC 7172	S2	0.0087	33.9		5.99 ± 0.50	42.92	13	15
MR 2251−178	S1	0.0640			4.75 ± 0.48	44.62	<1	27
NGC 7469	S1.2	0.0163			4.74 ± 0.78	43.40	<1	3
Mrk 926	S1.5	0.0469			3.56 ± 0.53	44.21	<1	3

luminosity function and absorption distribution. We also discuss the implications for the cosmological evolution of AGN and for the cosmic X-ray background. We note that there have been previous attempts to use INTEGRAL for studying the statistics and demography of nearby AGN (Krivonos et al. 2005; Bassani et al. 2006; Beckmann et al. 2006). The significant advantage of our present study is that it is based on an all-sky, largely serendipitious survey, which allowed us to significantly alleviate the previously significant bias associated with INTEGRAL AGN pointings. We also note that a similar all-sky

Table 1. continued.

Object (sources at $\|b\| < 5^\circ$ are given in bold)	Class[a]	z	D Mpc	Note[b]	$F_{17-60\ \mathrm{keV}}$ 10^{-11} erg/s/cm^2	$\log L_{\mathrm{hx}}$ erg/s	N_{H} 10^{22}cm^{-2}	Ref.[c]
Blazars								
87GB 003300.9+593328	Bl	0.0860			1.03 ± 0.15	44.22	<1	1
S5 0836+71	Bl	2.1720			3.47 ± 0.33	48.03	<1	1
PKS 1219+04	Bl	0.9650			1.30 ± 0.23	46.74	<1	4
3C 273	Bl	0.1583			13.83 ± 0.23	45.92	<1	1
3C 279	Bl	0.5362			1.50 ± 0.28	46.18	<1	1
Mrk 501	Bl	0.0337			4.53 ± 0.43	44.02	<1	1
PKS 1830−211	Bl	2.5070			3.35 ± 0.22	48.17	<1	25
BL Lac	Bl	0.0686			1.88 ± 0.38	44.28	<1	1
3C 454.3	Bl	0.8590			13.92 ± 0.55	47.64	<1	1
Transiently detected AGN								
NGC 0526A	S1.5	0.0191			3.72 ± 0.97	43.43		
ESO 297-G018	S2	0.0252			4.41 ± 0.94	43.75		
NGC 1052	S2	0.0050	17.8		2.12 ± 0.43	41.91		
IGR J03334+3718	S1	0.0547		18	1.96 ± 0.41	44.09		
LEDA 168563	S1	0.0290			4.42 ± 1.11	43.88		
AKN 120	S1	0.0327			8.38 ± 3.52	44.26		
MCG 8-11-11	S1.5	0.0205			5.61 ± 1.51	43.67		
IRAS 05589+2828	S1	0.0330			3.03 ± 0.62	43.83		
LEDA 096373	S2	0.0294			2.71 ± 0.61	43.68		
PG 0804+761	S1	0.1000			1.21 ± 0.33	44.43		
NGC 4051	S1.5	0.0023	17.0		2.11 ± 0.54	41.87		
NGC 4138	S1.9	0.0030	17.0		2.39 ± 0.49	41.92		
WAS 49B	S2	0.0630			0.95 ± 0.35	43.91		
NGC 4253	S1.5	0.0129			1.53 ± 0.31	42.70		
NGC 4258	S1.9	0.0015	6.8		1.90 ± 0.56	41.03		
XSS J12389−1614 = IGR J12391−1612	S2	0.0367		19	3.01 ± 0.62	43.92		
WKK 1263	S2	0.0244			1.28 ± 0.31	43.19		
PKS 1241-399	QSO	0.1910			1.77 ± 0.40	45.21		
Mrk 783	S1.5	0.0672			1.23 ± 0.32	44.08		
IGR J13038+5348 = MCG 09-21-096	S1	0.0299		18	2.11 ± 0.45	43.58		
NGC 5033	S1.9	0.0029	18.7		1.21 ± 0.28	41.71		
ESO 383-G018	S2	0.0124			1.74 ± 0.38	42.72		
NGC 5252	S1.9	0.0230			2.60 ± 0.78	43.44		
IGR J14175−4641	S2	0.0760		3	1.30 ± 0.28	44.21		
NGC 5548	S1.5	0.0172			2.06 ± 0.50	43.08		
ESO 511-G030	S1	0.0224			3.33 ± 0.91	43.53		
IGR J14471−6319	S2	0.0380		3	0.95 ± 0.23	43.45		
NGC 6240	S2	0.0245			4.66 ± 1.38	43.75		
3C 382	S1	0.0579			3.96 ± 1.75	44.45		
ESO 103-G035	S2	0.0133			6.64 ± 1.34	43.37		
XSS J19459+4508 = IGR J19473+4452	S2	0.0532		20	1.52 ± 0.45	43.96		
3C 403	NLRG	0.0590			0.96 ± 0.33	43.85		
4C +74.26	BLRG	0.1040			3.93 ± 1.22	44.98		
S5 2116+81	S1	0.0840			2.91 ± 0.98	44.65		
NGC 7314	S1.9	0.0048			2.17 ± 0.58	41.99		
Mrk 915	S1	0.0241			2.62 ± 0.56	43.49		

[a] Optical AGN class: Bl – blasar (BL Lac object or flat-spectrum radio quasar), S1, S1.2, S1.5, S1.8, S1.9, S2 – Seyfert galaxy, NLS1 – narrow-line Seyfert 1 galaxy, BLRG – broad-line radio galaxy, NLRG – narrow-line radio galaxy, QSO – quasar. [b] Note or reference for INTEGRAL discovered AGN: (1) Burenin et al. (2006b), (2) Sazonov et al. (2005), (3) Masetti et al. (2006d), (4) galaxy = 1RXS J094436.5−263353, a Seyfert 1 nucleus is suggested by the 6dF spectrum, (5) Morelli et al. (2006), =SWIFT J1038.8−4942, (6) Masetti et al. (2006a), (7) SDSS spectrum indicates a Seyfert 2 nucleus, (8) Swift localization consistent with this galaxy, (9) Revnivtsev et al. (2006), (10) Bassani et al. (2005), (11) Torres et al. (2004), (12) Masetti et al. (2004), (13) Bikmaev et al. (2006), (14) Masetti et al. (2006b), (15) Kennea et al. (2006), (16) Masetti et al. (2006c), (17) Bassani et al. (2006), (18) Burenin et al. (2006), (19) =2MASX J12390630−1610472 (Sazonov et al. 2005; Masetti et al. 2006a), (20) =2MASX J19471938+4449425 (Sazonov et al. 2005; Bikmaev et al. 2006; Masetti et al. 2006b). [c] Quoted N_{H} value or limit is adopted from or based on: (1) Donato et al. (2005), (2) RXTE data, (3) ASCA data, (4) ROSAT data, (5) Reynolds et al. (1997), (6) Matt et al. (2000), (7) Malizia et al. (1997), (8) Swift data, (9) Risaliti et al. (2005), N_{H} is strongly variable, (10) Lewis et al. (2005), (11) Vignali et al. (1998), (12) Immler et al. (2003), complex X-ray absorption, (13) Sazonov et al. (2005), (14) Risaliti et al. (2002), (15) Sazonov & Revnivtsev (2004), (16) Swift data, it is also possible that the X-ray spectrum is reflection-dominated with $N_{\mathrm{H}} > 10^{24}$ (Ajello et al. 2006), (17) Vignali et al. (2002), (18) Moran et al. (2005), (19) Woudt et al. (1998), (20) Levenson et al. (2001), (21) Bassani et al. (2005), (22) Sazonov et al. (2004b), (23) Einstein data, (24) assumed upper limit based on Seyfert 1 classification, (25) Oshima et al. (2001), (26) Young et al. (2002), (27) Reeves & Turner (2000).

hard X-ray survey has since recently been carried out by the Swift observatory (Markwardt et al. 2005).

2. The AGN sample

The catalog of Krivonos et al. (2006) includes in total 127 AGN, which are listed in Table 1. Of these, 91 AGN (referred to below as the main sample) were detected with more than 5σ significance on the time-averaged all-sky map obtained with IBIS/ISGRI in the 17–60 keV energy band and are thus well-suited for statistical analysis. In addition, there are 36 AGN, listed in the lower part of Table 1, that were confidently detected in single INTEGRAL orbits or observations (∼1–3 days long) but fall below the 5σ threshold on the average map. We exclude these transiently detected AGN from the following statistical analysis.

Most of the AGN presented were known as such before INTEGRAL, while 33 sources (those with "IGR" names) have been identified as AGN primarily based on their hard X-ray detection with INTEGRAL. Two of these newly discovered AGN – IGR J09446−2636 and IGR J13149+4422 – are reported here for the first time. As indicated in Col. 2 of Table 1, 77 objects in our main sample are optically classified as Seyfert galaxies (4 of them radio loud) and 9 are blazars (BL Lac objects or flat-spectrum radio quasars). Although the optical class has not yet been reported for 5 objects, their X-ray, optical, infrared, and radio properties strongly suggest that they are all Seyfert galaxies. The quoted optical classes are based on the NED unless a

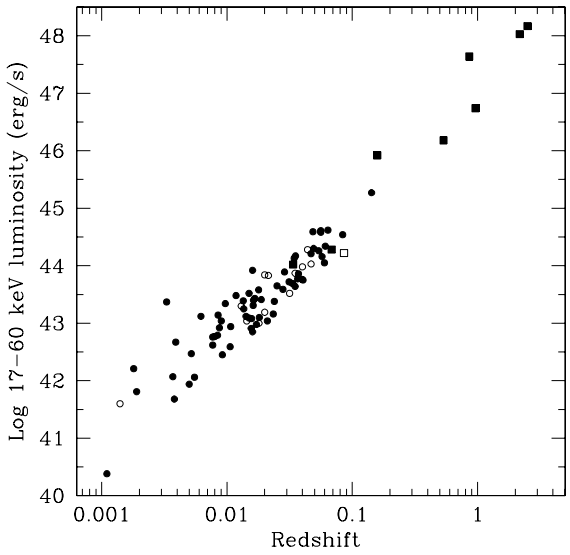

Fig. 1. Hard X-ray luminosity vs. redshift for the identified AGN from the INTEGRAL all-sky survey (the main sample). Circles and squares indicate emission-line AGN and blazars, respectively. Empty symbols indicate AGN located at $|b| < 5°$, which are not used in the statistical analysis.

reference is provided. Of the AGN at $|b| > 10°$ in our main sample, 30 were also detected during the RXTE Slew Survey.

We found published redshifts for all but 4 of our AGN (Col. 3 of Table 1) and used these to determine the source luminosities in the observed 17–60 keV energy band (Col. 7) from the hard X-ray fluxes measured by IBIS/ISGRI (Col. 6). For the nearest sources ($z \lesssim 0.01$) the distances from the Nearby Galaxies Catalogue (Tully 1988) were adopted (Col. 4), while the luminosity distances to the other objects were determined from their redshifts assuming a cosmology with $\Omega_m = 0.3$, $\Omega_\Lambda = 0.7$, and $H_0 = 75$ km s^{-1} Mpc^{-1}, which is used throughout the paper. Figure 1 shows the distribution of our AGN (of the main sample) in the redshift-luminosity plane. One can see that all of the emission-line (i.e. non-blazar) AGN are located at $z < 0.1$, except for IGR J09446−2636 at $z \approx 0.14$, while there are several blazars as distant as $z \sim$1–2.5, with (isotropical) luminosities up to $\sim 10^{48}$ erg s^{-1}. Because of the proximity of the non-blazar AGN, our quoted values for their observed luminosities may also be regarded as their rest-frame 17–60 keV luminosities.

We also collected information on the X-ray absorption columns for the AGN of the main sample (Col. 8 of Table 1). For this purpose we either used the literature or analyzed publicly available spectral data from different X-ray instruments, including ASCA/GIS, Einstein/IPC, RXTE/PCA, and Swift/XRT. The spectral modelling was done with XSPEC v12 (Arnaud 1996). The X-ray spectra (usually above 2 keV) were fitted by a model consisting of a power law photoabsorbed by a column N_H of neutral material and a fluorescent neutral-iron emission line at rest energy 6.4 keV if the latter was required by the fit (model zphabs × (powerlaw + Gaussian) in XSPEC). If the quality of the data allowed, we considered the power-law slope a free parameter; otherwise, the photon index was fixed at the canonical (e.g. Reynolds et al. 1997; Turner et al. 1997) AGN value $\Gamma = 1.8$. Note that we did not try to evaluate N_H if it was clear that $N_H < 10^{22}$ cm^{-2} (after subtraction of the Galactic absorption), as we regard such sources as unobscured throughout the paper. Finally, for several Seyfert 1 galaxies in our sample, which are expected to have little X-ray absorption, we used ROSAT/PSPC soft X-ray data to verify that indeed $N_H < 10^{22}$ cm^{-2} for them.

2.1. Unidentified sources

There are 24 unidentified sources among those detected on the average IBIS/ISGRI map (Krivonos et al. 2006), so our all-sky AGN sample can be significantly incomplete. However, since most of these objects are located close to the Galactic plane, we can optimize our statistical analysis by excluding the Galactic plane region $|b| < 5°$ from consideration. This leads to only a small decrease in the number of identified AGN – to 74, but to a dramatic reduction of the number of unidentified sources – to 7. The coordinates and fluxes of these high Galactic-latitude sources – AGN candidates – are given in Table 2. We note that the apparently high sky density of unidentified sources in the direction $l \sim 330°$, $b \sim 10°$ is probably the result of the extensive INTEGRAL observations of the Galactic plane and of such interesting sources as Cen A, NGC 4945, and SN 1006.

The treatment that follows is thus based on the $|b| > 5°$ AGN sample. Furthermore, we restrict our consideration to the emission-line AGN (66 in total) and so do not discuss blazars anymore.

3. X-ray absorption distribution

We first address the X-ray absorption distribution of nearby ($z \lesssim 0.1$) emission-line AGN. One of the most important findings of the RXTE Slew Survey was that the fraction of significantly X-ray absorbed AGN ($\log N_H > 22$) drops with increasing luminosity (Sazonov & Revnivtsev 2004). Motivated by this result, we divided our current INTEGRAL sample into two parts: AGN with $\log L_{hx} < 43.6$ and those with $\log L_{hx} > 43.6$, where L_{hx} is the luminosity in the 17–60 keV band. The chosen dividing luminosity approximately corresponds to the value of the 3–20 keV luminosity ($\log L_x = 43.5$) that we used in the RXTE case given that typically $\log(L_{hx}/L_x) \sim 0.1$ for local AGN, as will be shown in Sect. 4.3 below. This boundary also approximately corresponds to the bend of the hard X-ray luminosity function (Sect. 4). The resulting low- and high-luminosity samples include 42 and 24 objects, respectively.

Figure 2 shows the observed N_H distributions for these subsamples. It can be seen that, while ∼66% of local $\log L_{hx} < 43.6$ AGN are obscured ($\log N_H > 22$), the corresponding fraction is only ∼24% among the higher luminosity AGN. This result confirms our XSS finding but it is obtained here in a more straightforward manner. In the INTEGRAL case, the efficiency of source detection at energies above ∼20 keV is practically independent of intrinsic source absorption, as long as $\log N_H \lesssim 24.5$. In the XSS case, the detection was based on 3–20 keV fluxes, so we had to correct the observed N_H distribution for the significant loss in sensitivity to sources with $\log N_H > 23$.

We note that the above conclusion with respect to the fraction of obscured AGN as a function of luminosity is unlikely to change once the absorption columns are measured for those INTEGRAL AGN for which this information is not available yet, since there are only 4 and 3 such sources out of the 42 low- and 24 high-luminosity AGN, respectively (see Fig. 2).

We point out that the observed (see Fig. 2) small fraction of substantially Compton-thick AGN – sources with $\log N_H \gtrsim 24.5$ – should be interpreted with caution, since in their case the intrinsic hard X-ray flux is expected to be substantially suppressed by Comptonization on the cold material obscuring the AGN. The

Table 2. Unidentified INTEGRAL sources at $|b| > 5°$.

Source	RA (J2000.0)	Dec	l	b	$F_{17-60\ \mathrm{keV}}$ 10^{-11} erg/s/cm^2	Likely associations
IGR J02466-4222	41.65	–42.37	253.48	–62.07	3.08 ± 0.55	
IGR J09522-6231	148.05	–62.52	283.83	–6.50	1.17 ± 0.21	
IGR J13107-5551	197.68	–55.87	305.66	6.90	1.85 ± 0.30	XMMSL1 J131042.6-555206 (Read et al. 2005) = PMN J1310-5552
IGR J14561-3738	224.04	–37.65	328.61	18.93	1.40 ± 0.26	XSS J14562-37
IGR J16500-3307	252.51	–33.10	349.73	7.34	1.61 ± 0.23	1RXS J164955.1-330713
IGR J16562-3301	254.06	–33.03	350.60	6.37	1.97 ± 0.21	SWIFT J1656.3-3302 (Tueller et al. 2006)
IGR J17350-2045	263.75	–20.76	5.69	6.36	1.29 ± 0.18	

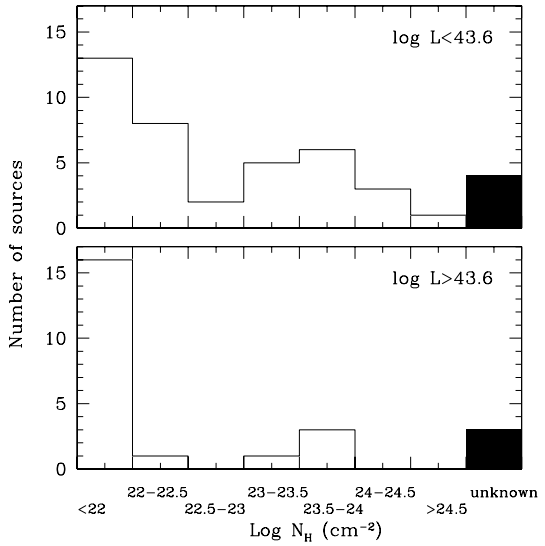

Fig. 2. Observed X-ray absorption distribution of the low-luminosity AGN (*top panel*), and high-luminosity AGN (*bottom panel*). The shaded part of each diagram shows the number of AGN with unknown $N_{\rm H}$.

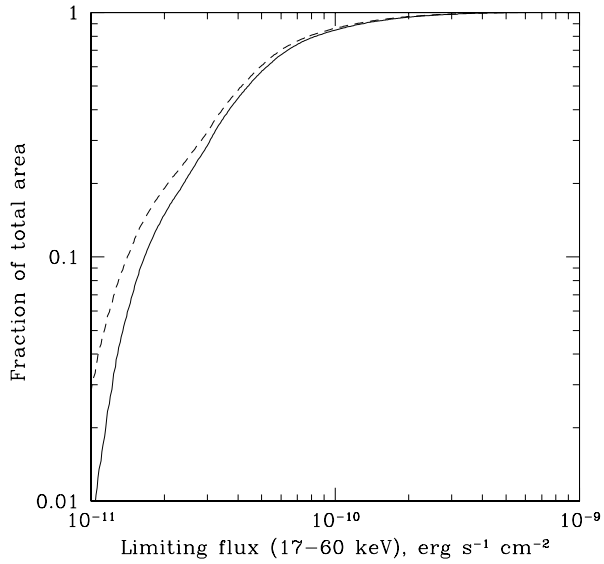

Fig. 3. Fraction of the total sky area as a function of survey sensitivity (the dashed line). The solid line shows the corresponding fraction for the $|b| > 5°$ sky.

discussion of the fraction of Compton-thick AGN in the local Universe will be continued in Sect. 6.

4. Hard X-ray luminosity function

We now define the hard X-ray luminosity function of nearby emission-line AGN as $\phi(L_{\rm hx}) \equiv {\rm d}N_{\rm AGN}/{\rm d}\log L_{\rm hx}$. We first estimated $\phi(L_{\rm hx})$ in binned form using the $1/V_{\rm m}$ method (Schmidt 1968), i.e. by summing $1/V_{\rm m}(L_{\rm hx,i})$ values for our AGN in specified luminosity intervals, where $V_{\rm m}(L_{\rm hx,i})$ is the space volume in which an AGN with luminosity $L_{\rm hx,i}$ could be detected by the survey. The $V_{\rm m}$ calculation was based on the dependence of the sky area covered by the survey on the achieved sensitivity, which is shown in Fig. 3. We note that ∼75% and ∼50% of the $|b| > 5°$ sky have been covered down to 5 and 3 mCrab, respectively, where 1 mCrab corresponds to $\sim 1.4 \times 10^{-11}$ erg s cm^{-2} (17–60 keV). The corresponding fractions are somewhat higher for the whole sky due to the overexposure of the Galactic plane region by INTEGRAL.

We performed the calculation in the luminosity range $40 < \log L_{\rm hx} < 45.5$, which includes all of our emission-line AGN, 66 objects in total. The resulting binned luminosity function with estimated 1σ statistical errors is shown in Fig. 4.

We next sought an analytic representation of the luminosity function in the form of a smoothly broken power-law model, as is conventional in AGN research:

$$\phi(L_{\rm hx}) = \frac{A}{(L_{\rm hx}/L_*)^{\gamma_1} + (L_{\rm hx}/L_*)^{\gamma_2}}. \quad (1)$$

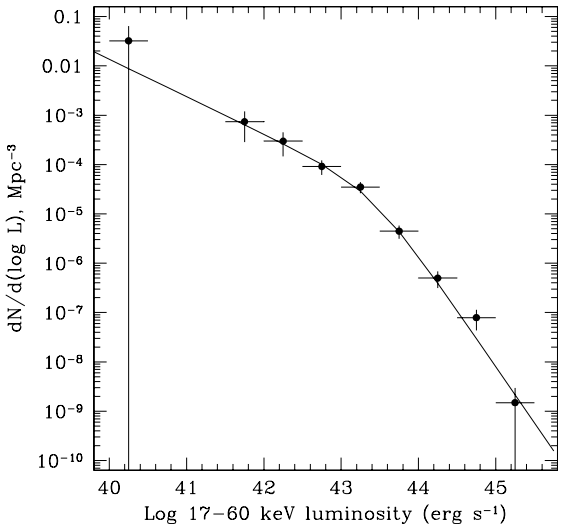

Fig. 4. Hard X-ray luminosity function of local emission-line AGN obtained with INTEGRAL in binned form (solid circles and 1σ error bars). The solid line shows the analytic approximation given by Eq. (1) and Table 3.

For this purpose we used the maximum likelihood estimator

$$L = -2 \sum_i \ln \frac{\phi(L_{{\rm hx},i}) V_{\rm m}(L_{{\rm hx},i})}{\int \phi(L_{\rm hx}) V_{\rm m}(L_{\rm hx})\, {\rm d}\log L_{\rm hx}}, \quad (2)$$

where i runs over all sampled AGN.

Table 3. Parameters of the hard X-ray luminosity function.

Parameter	Value and 1σ range
$\log L_*$	43.40 (43.12 ÷ 43.68)
γ_1	0.76 (0.56 ÷ 0.94)
γ_2	2.28 (2.06 ÷ 2.56)
A (Mpc^{-3})	3.55×10^{-5}
$n_{17-60\ \mathrm{keV}}(>40)$ (10^{-3} Mpc^{-3})	9 (4 ÷ 18)
$n_{17-60\ \mathrm{keV}}(>41)$ (10^{-3} Mpc^{-3})	1.4 (0.9 ÷ 2.0)
$\rho_{17-60\ \mathrm{keV}}(>40)$ (10^{38} erg s^{-1} Mpc^{-3})	14.1 (11.8 ÷ 17.1)
$\rho_{17-60\ \mathrm{keV}}(>41)$ (10^{38} erg s^{-1} Mpc^{-3})	12.4 (11.0 ÷ 14.0)
P_{KS}	>0.9

By minimizing L, we found the best-fit values for the break luminosity L_*, as well as for the slopes γ_1 and γ_2. Since the maximum likelihood method directly determines only the shape of the function, we derived the normalization A by requiring that the number of AGN predicted by the model be equal to the number of AGN in the sample. The resulting best-fit model is shown in Fig. 4 and its parameters are given in Table 3 together with their estimated 1σ errors; the error for the coefficient A is not quoted, since this parameter is strongly correlated with the others. The analytic fit is apparently in good agreement with the binned $\phi(L_{\mathrm{hx}})$, and the good quality of the fit is confirmed by the Kolmogorov-Smirnov test.

4.1. Cumulative number density and luminosity density

By integrating the derived luminosity function over luminosity, we can find the total number density of nearby emission-line AGN with $\log L_{\mathrm{hx}} > 40$:

$$n(>40) = \int_{40}^{\infty} \phi(L_{\mathrm{hx}})\, \mathrm{d} \log L_{\mathrm{hx}}. \quad (3)$$

The resulting value is given in Table 3, together with its 1σ uncertainty range. It should be noted that this cumulative number density is strongly dominated by AGN at the low end of the probed luminosity range and that there is only one AGN in our sample (NGC 4395) with $\log L_{\mathrm{hx}} < 41$. For this reason we also provide our estimate of (similarly defined) $n(>41)$ in Table 3.

We can also determine the cumulative luminosity density of nearby emission-line AGN with $\log L_{\mathrm{hx}} > 40$:

$$\rho_{17-60\ \mathrm{keV}}(>40) = \int_{40}^{\infty} \phi(L_{\mathrm{hx}}) L_{\mathrm{x}}\, \mathrm{d} \log L_{\mathrm{hx}}. \quad (4)$$

The result is presented in Table 3. Also given in the table is the value of $\rho_{17-60\ \mathrm{keV}}(> 41)$, which is better constrained by the data.

4.2. Systematic uncertainties

There are some systematic effects that may affect the luminosity function obtained. First, our input AGN sample may be incomplete because there are 7 unidentified INTEGRAL sources at $|b| > 5^\circ$, some of which may eventually prove to be emisison-line AGN. Assuming that there is no strong luminosity bias for these sources, the amplitude of our luminosity function can be underestimated due to incompleteness by $\sim$10% at most.

Another cause of concern is that 15 of our $|b| > 5^\circ$ emission-line AGN have been at least once the target of a pointed INTEGRAL observation, i.e. we are not dealing with a truly serendipitous survey. In order to assess the maximum possible systematic effect associated with these AGN pointings, the following argument can be suggested. Suppose that an area S of the sky was covered by the survey down to flux f_1 or lower, while the total area of the survey is S_0. Suppose next that a total of N sources with flux $f_1 < f < f_2$ were detected, of which N_{t} were observational targets. Then the sky density ρ of sources with $f_1 < f < f_2$ can be expected to be bound in the range ($\rho_{\min} < \rho < \rho_{\max}$):

$$\frac{N - N_{\mathrm{t}}}{S} + \frac{N_{\mathrm{t}}}{S_0} < \rho < \frac{N}{S}. \quad (5)$$

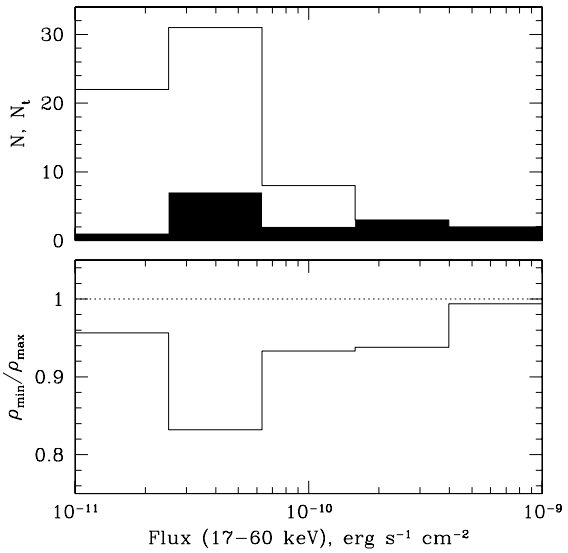

Fig. 5. *Top*: differential distribution of hard X-ray fluxes for all INTEGRAL emission-line AGN at $|b| > 5^\circ$ (upper histogram) and only for those targeted by INTEGRAL (filled histogram). *Bottom*: the ratio of the minimum and maximum estimates of the sky density of sources according to Eq. (5).

Our calculation of the luminosity function was implicitly based on using $\rho_{\max}$. Figure 5 shows the ratio $\rho_{\min}/\rho_{\max}$ as a function of flux for our AGN survey. It can be seen that the effect under consideration is strongest at medium fluxes (~ 2–6×10^{-11} erg s^{-1} cm^{-2}) where the fraction of targeted AGN is relatively high, while the sky coverage is relatively low. However, even at the maximum the effect is less than 17%. This value can be considered an upper limit on the possible overestimation of the luminosity function due to the presence of targeted AGN in the sample. We note that implementing observations of "empty" extragalactic regions with INTEGRAL (Proposal 0320108) has allowed us to significantly reduce the non-randomness of the survey.

We may conclude from the above that the total systematic uncertainty in the luminosity function due to source identification incompleteness and AGN pointings is probably $\lesssim$10% (taking into account that the two effects tend to counterbalance each other), which is less than the present statistical uncertainties.

Finally, the standard V/V_{m} test (Schmidt 1968) applied to our AGN sample demonstrates (Fig. 6) that the spatial distribution of the studied AGN population is consistent with being homogeneous.

4.3. Comparison with the 3–20 keV luminosity function

It is interesting to compare the local AGN luminosity function obtained with INTEGRAL in the hard X-ray band (17–60 keV) with that previously constructed in the adjacent, medium X-ray

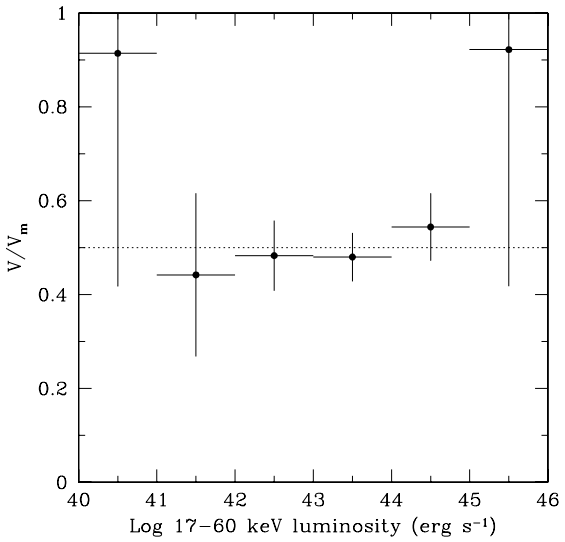

Fig. 6. $V/V_{\rm m}$ ratio averaged over luminosity bins for the AGN sample used for the construction of the luminosity function. The error bars represent 1σ statistical uncertainties.

band (3–20 keV) using the RXTE Slew Survey (Sazonov & Revnivtsev 2004).

For this comparison we need to know how the 17–60 keV luminosities ($L_{\rm hx}$) of Seyfert galaxies are related to their 3–20 keV luminosities ($L_{\rm x}$). One possibility is to directly compare $L_{\rm hx}$ with $L_{\rm x}$ for those emission-line AGN detected during both the XSS and the INTEGRAL all-sky survey. We have in total 25 such cases, for which we show in Fig. 7 $L_{\rm x}$ vs. $L_{\rm hx}$ and the ratio $L_{\rm x}/L_{\rm hx}$ as a function of $N_{\rm H}$. These data are compared with the expected dependence of $L_{\rm x}/L_{\rm hx}$ on $N_{\rm H}$ assuming that the intrinsic (unabsorbed) AGN spectrum consists of a power law with a photon index $\Gamma = 1.8$ plus a Compton reflection component (XSPEC model pexrav, Magdziarz & Zdziarski 1995) of different relative amplitudes $R(\equiv\Omega/2\pi$, for a zero inclination angle). As expected (see the upper panel of Fig. 7), for most of the AGN $L_{\rm x} < L_{\rm hx}$ mainly due to the presence of intrinsic X-ray absorption and (to a lesser degree) of Compton reflection. The measured $L_{\rm x}/L_{\rm hx}$ ratios are apparently consistent with the expected $N_{\rm H}$ trend, somewhat more so in the case of a non-negligible reflection component ($R \sim 0.5$–1). The observed significant (a factor of ∼2) scatter of the data around this trend can be naturally explained by intrinsic variability of the sources, since the RXTE and INTEGRAL observations are separated by years.

Taking the outcome of this test into account and considering the abundant literature on the broad-band X-ray spectra of Seyfert galaxies (e.g. Gondek et al. 1996; Perola et al. 2002), we may adopt to a first approximation that local emission-line AGN have a universal intrinsic spectrum consisting of a power law with $\Gamma = 1.8$ and a substantial reflection component ($R \sim 0.5$–1). We can then estimate the average ratio $\langle L_{\rm x}/L_{\rm hx}\rangle$ for low- ($\log L_{\rm hx} < 43.6$) and high- ($\log L_{\rm hx} > 43.6$) luminosity AGN taking their (different) observed $N_{\rm H}$ distributions (Fig. 2) into account. For the low-luminosity AGN, we find $\langle L_{\rm x}/L_{\rm hx}\rangle = 0.79$ (0.67) for $R = 0.5$ (1). For the high-luminosity AGN, most of which are unobscured, the corresponding values are 0.96 (0.84). Note that, in this context, changing the reflection amplitude R by 0.5 corresponds to changing the power-law slope by ∼0.1. Given the above numbers, we may adopt to a first approximation that $\log\langle L_{\rm hx}/L_{\rm x}\rangle \approx 0.1$ regardless of luminosity, and accordingly convert the XSS luminosity function to the 17–60 keV band.

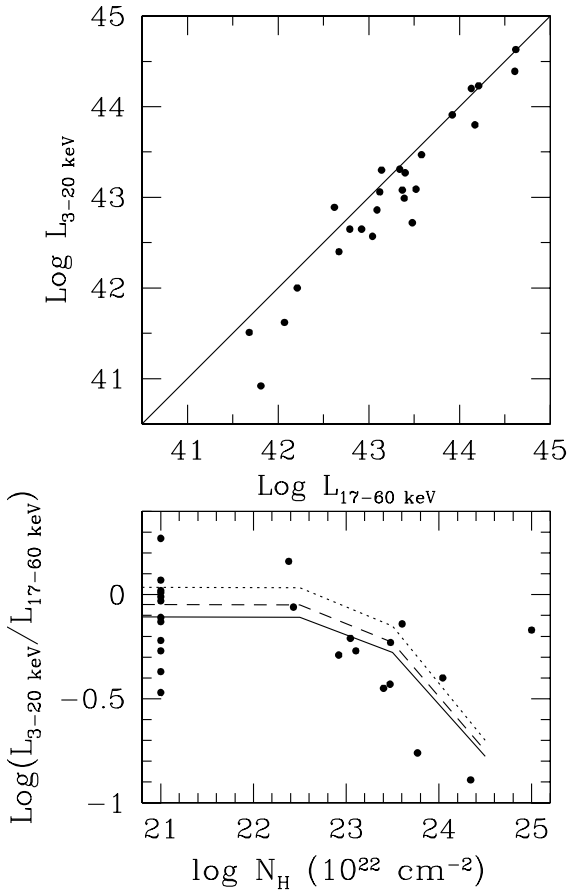

Fig. 7. *Top*: the 3–20 keV luminosity as a function of 17–60 keV luminosity for AGN detected during both the RXTE Slew Survey and INTEGRAL all-sky survey. The line indicates equality of the two luminosities. *Bottom*: the 3–20 keV/17–60 keV luminosity ratio as a function of $N_{\rm H}$ (points). The data shown at $\log N_{\rm H} = 21$ represent unobscured AGN ($\log N_{\rm H} < 22$). Also shown are expected luminosity ratios in the absence of source variability for an intrinsic (unabsorbed) spectrum consisting of a power law ($\Gamma = 1.8$) and a Compton reflection component with relative amplitude $R = 0$ (dotted line), $R = 0.5$ (dashed line), and $R = 1$ (solid line).

The result is shown in Fig. 8 in comparison with the hard X-ray luminosity function measured directly by INTEGRAL. Note that the amplitude and error bars for the XSS luminosity function take into account the systematic uncertainty due to possible incompleteness of the XSS sample of AGN (Sazonov & Revnivtsev 2004). The two luminosity functions agree with each other, as is formally confirmed by a comparison of the parameters of the best-fit analytic models. However, there is an indication that the XSS luminosity function lies somewhat below the INTEGRAL one. Here it is best to consider the cumulative luminosity density. With RXTE we measured $\rho_{3-20\ {\rm keV}}(>41) = (5.2 \pm 1.2) \times 10^{38}$ erg s^{-1} Mpc^{-3}, which for the $\langle L_{\rm hx}/L_{\rm x}\rangle$ ratio adopted above implies that $\rho_{17-60\ {\rm keV}}(>41.1) = (6.5 \pm 1.5) \times 10^{38}$ erg s^{-1} Mpc^{-3}. With INTEGRAL we found $\rho_{17-60\ {\rm keV}}(>41) = (12.4 \pm 1.5) \times 10^{38}$ erg s^{-1} Mpc^{-3}, i.e. a factor of 1.9 ± 0.5 higher luminosity density.

5. Implications for the cosmic X-ray background

It has become a common paradigm that the bulk of the cosmic X-ray background (CXB) is composed of emission from all AGN in the Universe. This conclusion is mainly based on the

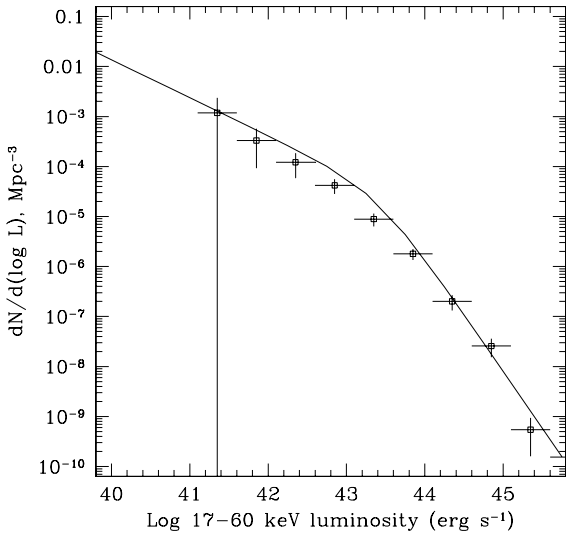

Fig. 8. The best-fit model of the hard X-ray AGN luminosity function obtained with INTEGRAL (line) in comparison with the luminosity function based on the RXTE Slew Survey in the 3–20 keV band (Sazonov & Revnivtsev 2004), here converted to the 17–60 keV band (points with error bars).

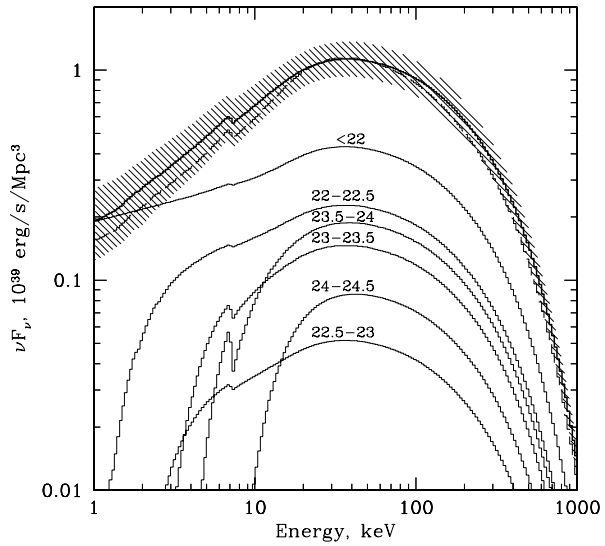

Fig. 9. Composite spectrum of the local emission-line AGN obtained assuming that the intrinsic AGN spectrum is given by Eq. (7) with $\Gamma = 1.8$, $E_\mathrm{f} = 200$ keV, and $R = 0.5$ (thick solid line), and taking the observed N_H distribution of nearby AGN (Fig. 2) into account. The spectrum is normalized to the measured local AGN 17–60 keV luminosity density. The shaded area indicates the uncertainty in the composite spectrum due to the uncertainties in the $\rho_{17-60\ \mathrm{keV}}(>40)$ value and in the N_H distribution. Also shown are the contributions to the composite spectrum of AGN with different degrees of obscuration (curves with labels indicating $\log N_\mathrm{H}$). The dashed line shows the composite spectrum in the case of $R = 1$.

fact that deep extragalactic X-ray surveys have resolved ∼80% of the CXB at energies below ∼8 keV (Hickox & Markevitch 2006). However, the maximum of the CXB νF_ν spectrum is located at ∼30 keV, and at these energies not more than ∼3% of the CXB has been resolved into point sources in the deepest exposures with INTEGRAL (and much less by previous missions). Therefore, resolving the CXB near its peak will be one of the main tasks of future hard X-ray missions. For the time being, it is interesting to address the following question: is the X-ray absorption distribution measured with INTEGRAL for the local AGN population consistent with that required for distant quasars to explain the CXB spectrum?

To answer this question, we can deduce relative fractions of AGN with different absorption columns from the measured local N_H distribution (Fig. 2):

$$\begin{aligned}
\log N_\mathrm{H} &< 22.0: \quad 0.37 \pm 0.10,\\
22.0 < \log N_\mathrm{H} &< 22.5: \quad 0.20 \pm 0.07,\\
22.5 < \log N_\mathrm{H} &< 23.0: \quad 0.05 \pm 0.04,\\
23.0 < \log N_\mathrm{H} &< 23.5: \quad 0.13 \pm 0.06,\\
23.5 < \log N_\mathrm{H} &< 24.0: \quad 0.16 \pm 0.07,\\
24.0 < \log N_\mathrm{H} &< 24.5: \quad 0.07 \pm 0.05,\\
\log N_\mathrm{H} &> 24.5: \quad 0.02 \pm 0.02.
\end{aligned} \tag{6}$$

These fractions take into account that low- ($\log L_\mathrm{hx} < 43.6$) and high- ($\log L_\mathrm{hx} > 43.6$) luminosity AGN contribute ∼90% and ∼10%, respectively, to the local luminosity density. The quoted errors result from Poissonian statistics and we have ignored the systematic uncertainty associated with the lack of N_H measurements for several AGN in our sample.

We next adopt a fiducial intrinsic AGN spectrum consisting of a cutoff power-law component and the corresponding Compton reflection component with relative amplitude R:

$$\frac{\mathrm{d}N_\gamma}{\mathrm{d}E} = AE^{-\Gamma}\exp(-E/E_\mathrm{f}) + Rf(E), \tag{7}$$

where $f(E)$ is again described by the pexrav model (Magdziarz & Zdziarski 1995). We adopt $\Gamma = 1.8$, $E_\mathrm{f} = 200$ keV, and $R = 0.5$ or $R = 1$ as reference values.

We can now build the composite spectrum of the local AGN by propagating the intrinsic spectrum given by Eq. (7) through different absorption columns and summing up the resulting spectra with the weights introduced in Eq. (6). The resulting spectrum is shown in Fig. 9. Note that we have neglected the contribution of substantially Compton-thick AGN ($\log N_\mathrm{H} > 24.5$) since it is expected to be small (∼3%) given the observed N_H distribution (Fig. 2), whereas the spectra of Compton-thick AGN can assume quite different shapes depending on the geometry of the obscuring and reflecting material (e.g. Matt et al. 2000).

The composite spectrum shown in Fig. 9 has been normalized so as to reproduce the local AGN luminosity density measured with INTEGRAL, $\rho_{17-60\ \mathrm{keV}}(>40)$ (Table 3), i.e. this spectrum represents the volume emissivity of all local emission-line AGN with $\log L_\mathrm{hx} > 40$. In Fig. 9 we indicate the range of uncertainty in the composite spectrum resulting from the uncertainties in the N_H distribution and in the $\rho_{17-60\ \mathrm{keV}}(>40)$ value. It can also be seen that the difference between the normalized composite spectra for $R = 0.5$ and $R = 1$ is only noticeable below ∼15 keV.

Suppose now that the same spectral shape characterizes AGN at all redshifts and that only the AGN luminosity density evolves with z. Then the cumulative AGN emission observed at $z = 0$ will have a spectrum (for a flat cosmology, e.g. Sazonov et al. 2004a)

$$I(E) = \frac{c}{4\pi H_0}\int_0^\infty \frac{\epsilon(z)F((1+z)E)}{(1+z)\left[\Omega_\mathrm{m}(1+z)^3+\Omega_\Lambda\right]^{1/2}}\mathrm{d}z, \tag{8}$$

where $F(E)$ is the template spectrum shown in Fig. 9 and $\epsilon(z)$ is a function describing the evolution of the luminosity density.

The best constraints on $\epsilon(z)$ have so far been coming from deep X-ray surveys with Chandra and XMM-Newton. In Fig. 10 we reproduce the results of Barger et al. (2005) on the redshift dependence of the rest-frame 2–8 keV luminosity density of AGN, which reflects the observed pure luminosity evolution of

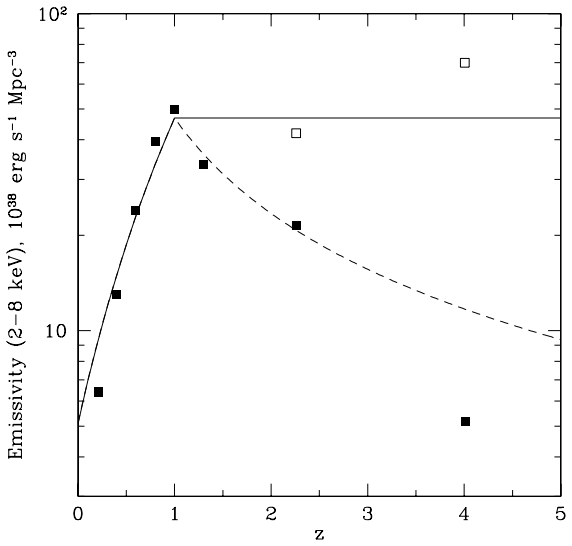

Fig. 10. Evolution with redshift of the rest-frame 2–8 keV luminosity density based on Chandra extragalactic surveys (adopted from Barger et al. 2005). The measurements shown by the filled squares take only spectroscopically identified AGN into account, while those shown by the empty squares also take the maximal incompleteness into account. We assume that the true evolution is bound between the two limiting functions given by Eqs. (9) and (10), shown by the dashed and solid lines, respectively.

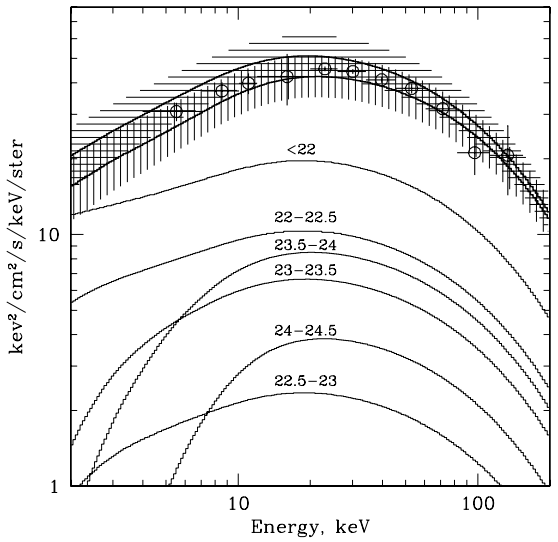

Fig. 11. Predicted CXB spectrum based on the local AGN composite spectrum (Fig. 9, for $R = 0.5$) and the AGN redshift evolution measured with Chandra (Fig. 10). The upper thick solid line corresponds to the scenario of flat AGN luminosity density evolution at $z > 1$, the horizontally shaded region indicating the corresponding uncertainty. The lower solid line and the vertically shaded region correspond to the scenario of $\propto 1/z$ evolution at $z > 1$. The other presented curves show the contributions of AGN with different degrees of obscuration (the labels indicate $\log N_{\rm H}$). The points with error bars show the CXB spectrum measured with the JET-X, IBIS/ISGRI, and SPI instruments on INTEGRAL (Churazov et al. 2006).

the AGN luminosity function at $z \lesssim 1.5$. Between $z \sim 0.2$ and $z \sim 1$ the evolution is well-constrained and is consistent with a power-law dependence (z^{α}) with a slope $\alpha \sim 3.2$. At $z \gtrsim 1$ there is still significant uncertainty due to the incompleteness of source identification and redshift determination, and the evolution function $\epsilon(z)$ is bound by the two sets of data points in Fig. 10, or approximately by the following two limiting functions, also shown in the figure:

$$e_1(z) \propto \begin{cases} (1+z)^{3.2}, & z \le 1 \\ e_1(1)/z, & z > 1 \end{cases} \quad (9)$$

$$e_2(z) \propto \begin{cases} (1+z)^{3.2}, & z \le 1 \\ e_2(1), & z > 1. \end{cases} \quad (10)$$

By convolving our locally-determined composite AGN spectrum (Fig. 9) with these two alternative evolution laws, we obtain the cumulative AGN spectra shown in Fig. 11. The shaded regions around these spectra represent the superposition of the present uncertainties in the local $\rho_{17-60\ \rm keV}(>40)$ value and in the local $N_{\rm H}$ distribution. For comparison in Fig. 11 the CXB broadband spectrum is shown as recently measured with the different instruments on INTEGRAL (Churazov et al. 2006). It can be seen that the predicted cumulative AGN spectrum agrees very well, both in amplitude and in shape, with the CXB for both limiting scenarios of AGN evolution at $z > 1$. It should be noted, though, that our calculation was based on the INTEGRAL estimate of the cumulative luminosity density of local AGN with $\log L_{\rm hx} > 40$, so the inclusion of even lower luminosity AGN and normal galaxies could somewhat increase the normalization of the predicted cumulative AGN spectrum.

We conclude that the combination of data from the INTEGRAL all-sky survey and deep extragalatic X-ray surveys seems to be able to naturally explain the observed CXB spectrum. Furthermore these data are consistent with the cosmological evolution of AGN at $z \lesssim 1.5$ (where the bulk of the CXB is produced) having occurred mostly in luminosity and much less (if any) in spectral properties such as the X-ray absorption distribution (for a given value of $L_{\rm hx}/L_*(z)$).

6. Conclusions

We have used the INTEGRAL all-sky hard X-ray survey to study some key properties of the local ($z \lesssim 0.1$) AGN population. Since our source detection was based on 17–60 keV fluxes, the survey is equally sensitive to AGN with X-ray absorption columns up to several 10^{24} cm^{-2}, i.e. well into the Compton-thick domain ($N_{\rm H} > 1.5 \times 10^{24}$ cm^{-2}).

One of the most surprising results of the survey is that very few Compton-thick AGN have been detected, and all of them were known before. The observed fraction of Compton-thick objects is only ~10%. This estimate may increase to at most ~20% once the currently missing absorption columns are measured. Clearly Compton-thick AGN are fairly rare. A note of caution is necessary here concerning very Compton-thick objects ($\log N_{\rm H} \sim 25$–26). Since their observed hard X-ray luminosities are expected to be $\lesssim$10% of their intrinsic luminosities, such sources may constitute a major fraction of AGN at luminosities near our survey's effective limit ($L_{\rm hx} \sim 10^{40}$–10^{41} erg s^{-1}) and below.

Another major result of our study is confirmation of the result of the RXTE Slew Survey that the local AGN absorption distribution is very different at low ($\log L_{\rm hx} < 43.6$) and high ($\log L_{\rm hx} > 43.6$) luminosities. While the fraction of obscured ($\log N_{\rm H} > 22$) objects is ~70% among the low-luminosity AGN, it is only ~25% among the high-luminosity ones. We note that a similar result was recently reported based on a combination of different HEAO-1 (2–10 keV) surveys (Shinozaki 2006) and is also emerging from the all-sky hard X-ray survey carried out by Swift (Markwardt et al. 2005). Furthermore, a similar trend has been found at higher redshifts (e.g. Ueda et al. 2003).

We measured the hard X-ray luminosity distribution of local emission-line AGN. Its broken power-law shape is in good agreement with recent determinations in softer energy bands, in particular at 3–20 keV (Sazonov & Revnivtsev 2004) and at 2–10 keV (Shinozaki 2006). We also found the cumulative luminosity density of AGN with $L_{\rm hx} > 10^{41}$ erg s^{-1} to be $\rho_{17-60\ {\rm keV}}(>41) = (12.4 \pm 1.5) \times 10^{38}$ erg s^{-1} Mpc^{-3}. This is a factor of $\sim$1.9 higher than the XSS measurement in the 3–20 keV band assuming that typically $\langle L_{17-60\ {\rm keV}}/L_{3-20\ {\rm keV}}\rangle \sim 1.25$. Thus the two determinations differ by $\sim 2.8\sigma$, although there is a significant uncertainty in the average ratio $\langle L_{17-60\ {\rm keV}}/L_{3-20\ {\rm keV}}\rangle$. Our INTEGRAL estimate of the AGN cumulative luminosity density in the 17–60 keV band also seems to be consistent with the 2–10 keV estimate of Shinozaki (2006): $\rho_{2-10\ {\rm keV}}(>42) = (7.2 \pm 1.4) \times 10^{38}$ erg s^{-1} Mpc^{-1} (for $H_0 = 75$ km s^{-1} Mpc^{-1}), given that on average $L_{17-60\ {\rm keV}}/L_{2-10\ {\rm keV}} \sim 2$. Finally, the hard X-ray luminosity function obtained in this work agrees with the one constructed by Beckmann et al. (2006) based on a smaller sample of INTEGRAL AGN, improving it in terms of accuracy and reducing the bias associated with AGN pointed observations.

In summary, the all-sky X-ray and hard X-ray surveys performed with RXTE, INTEGRAL, Swift, and HEAO-1 have provided an accurate census of nearby unobscured and obscured AGN. This new information is not only interesting in its own right but also provides a reliable $z = 0$ point for studies of AGN cosmological evolution and the growth of massive black holes.

As a first attempt to apply the local AGN statistics in a cosmological context, we demonstrated that the spectral shape and amplitude of the CXB allow for the possibility that the absorption distribution of AGN (for a given $L_{\rm hx}/L_*(z)$ ratio) has not changed significantly since $z \sim 1.5$, while the AGN luminosity function has experienced pure luminosity evolution. It should be noted that we came to this tentative conclusion using a fiducial (although realistic) intrinsic AGN spectrum. In future work we plan to perform a more self-consistent analysis by using INTEGRAL data on the hard X-ray spectra of nearby AGN. We also note that it is possible that the hard X-ray spectra of nearby Seyferts are in reality somewhat different from those of distant powerful quasars, since to a first approximation the intrinsic (unabsorbed) spectrum is expected to depend on the black hole mass, accretion rate (Shakura & Sunyaev 1976), and spin. Observations with future hard X-ray telescopes will permit direct tests of whether the hard X-ray spectra of quasars are similar to those of local Seyferts or not.

Acknowledgements. This work was partly supported by the DFG-Schwerpunktprogramme (SPP 1177), the program of the Russian Academy of Sciences "Origin and evolution of stars and galaxies", and grant of the President of Russia NSh-1100.2006.2. The research made use of the NASA/IPAC Extragalactic Database (operated by the Jet Propulsion Laboratory, California Institute of Technology), SIMBAD database (operated at the CDS, Strasbourg), and data of different X-ray astronomy missions obtained through the High Energy Astrophysics Science Archive Research Center Online Service, provided by the NASA/Goddard Space Flight Center. Some of the INTEGRAL sources were identified thanks to follow-up X-ray observations with Chandra and Swift/XRT. INTEGRAL is an ESA project funded by ESA member states (especially the PI countries: Denmark, France, Germany, Italy, Spain, Switzerland), Czech Republic and Poland, and with the participation of Russia and the USA.

References

Ajello, M., Greiner, J., Kupcu, et al. 2006, ATel, 864
Arnaud, K. A. 1996, Astronomical Data Analysis Software and Systems V, ed. G. Jacoby, & J. Barnes, ASP Conf. Ser., 101, 17
Barger, A. J., Cowie, L. L., Mushotzky, R. F., et al. 2005, AJ, 129, 578
Bassani, L., De Rosa, A., Bazzano, A., et al. 2005, ApJ, 634, L21
Bassani, L., Molina, M., Malizia, A., et al. 2006, ApJ, 636, L65
Beckmann, V., Soldi, S., Shrader, C. R., Gehrels, N., & Produit, N. 2006, ApJ, 638, 642
Bikmaev, I. F., Sunyaev, R. A., Revnivtsev, M. G., & Burenin, R. A. 2006, Astron. Lett., 32, 221
Brandt, W. N., & Hasinger, G. 2005, ARA&A, 43, 827
Burenin, R., Mescheryakov, A., Revnivtsev, M., Bikmaev, I., & Sunyaev, R. 2006, ATel, 880
Burenin, R., Mescheryakov, A., Sazonov, S., et al. 2006b, ATel, 883
Churazov, E., Sunyaev, R., Revnivtsev, M., et al. 2006, A&A, submitted [arXiv:astro-ph/0608250]
Donato, D., Sambruna, R. M., & Gliozzi, M. 2005, A&A, 433, 1163
Gondek, D., Zdziarski, A. A., Johnson, W. N., et al. 1996, MNRAS, 282, 646
Hickox, R. C., & Markevitch, M. 2006, ApJ, 645, 95
Immler, S., Brandt, W. N., Vignali, C., et al. 2003, AJ, 126, 153
Kennea, J., Pavlov, G. G., Bykov, A. M., et al. 2006, ATel, 788
Krivonos, R., Vikhlinin, A., Churazov, E., et al. 2005, ApJ, 625, 89
Krivonos, R., et al. 2006, in preparation
Levenson, N. A., Weaver, K. A., & Heckman, T. M. 2001, ApJS, 133, 269
Lewis, K. T., Eracleous, M., Gliozzi, M., Sambruna, R. M., & Mushotzky, R. F. 2005, ApJ, 622, 816
Magdziarz, P., & Zdziarski, A. A. 1995, MNRAS, 273, 837
Malizia, A., Bassani, L., Stephen, J. B., Malaguti, G., & Palumbo, G. G. 1997, ApJS, 113, 311
Markwardt, C. B., Tueller, J., Skinner, G. K., et al. 2005, ApJ, 633, L77
Masetti, N., Palazzi, E., Palazzi, E., Bassani, L., Malizia, A., & Stephan, J. B. 2004, A&A, 426, L41
Masetti, N., Pretorius, M. L., Palazzi, E., et al. 2006a, A&A, 449, 1139
Masetti, N., Mason, E., Bassani, L., et al. 2006b, A&A, 448, 547
Masetti, N., Bassani, L., Bazzano, A., et al. 2006c, A&A, 455, 11
Masetti, N., Morelli, L., Palazzi, E., et al. 2006d, A&A, 459, 21
Matt, G., Fabian, A. C., Guainazzi, M., et al. 2000, MNRAS, 318, 173
Molina, M., Bassani, L., Malizia, A., Stephen, J. B., & Bazzano, A., 2006, ATel, 263
Moran, E. C., Eracleous, M., Leighly, K. M., et al. 2005, AJ, 129, 2108
Morelli, L., Masetti, N., Bassani, L., et al. 2006, ATel, 785
Oshima, T., Mitsuda, K., Ota, N., et al. 2001, ApJ, 551, 929
Perola, G. C., Matt, G., Cappi, M., et al. 2002, A&A, 389, 802
Read, A. M., Saxton, R. D., Esquej, M. P., Freyberg, M. J., & Altieri, B. 2005, Proc. 2005 EPIC XMM-Newton Consortium Meeting, MPE Rep., 288, 137
Reeves, J. N., & Turner, M. J. L. 2000, MNRAS, 316, 234
Revnivtsev, M., Sazonov, S., Jahoda, K., & Gilfanov, M. 2004, A&A, 418, 927
Revnivtsev, M. G., Sazonov, S. Y., Molkov, S. V., et al. 2006, Astron. Lett., 32, 145
Reynolds, C. S. 1997, MNRAS, 286, 513
Risaliti, G., Elvis, M., & Nicastro, F. 2002, ApJ, 571, 234
Risaliti, G., Elvis, M., Fabbiano, G., Baldi, A., & Zezas, A. 2005, ApJ, 623, L93
Sazonov, S., & Revnivtsev, M. 2004, A&A, 423, 469
Sazonov, S. Y., Ostriker, J. P., & Sunyaev, R. A. 2004a, MNRAS, 347, 144
Sazonov, S. Y., Revnivtsev, M. G., Lutovinov, A. A., Sunyaev, R. A., & Grebenev, S. A. 2004b, A&A, 421, L21
Sazonov, S., Churazov, E., Revnivtsev, M., Vikhlinin, A., & Sunyaev, R. 2005, A&A, 444, L37
Schmidt, M. 1968, ApJ, 151, 393
Shakura, N. I., & Sunyaev, R. A. 1976, MNRAS, 175, 613
Shinozaki, K., Miyaji, T., Ishisaki, Y., Ueda, Y., & Ogasaka, Y. 2006, ApJ, 131, 2943
Torres, M. A. P., Garcia, M. R., McClintock, J. E., et al. 2004, ATel, 264
Tueller, J., Markwardt, C., Ajello, M., et al. 2006, ATel, 835
Tully, R. B. 1988, Nearby Galaxies Catalogue (Cambridge University Press)
Turner, T. J., George, I. M., Nandra, K., & Mushotzky, R. F. 1997, ApJS, 113, 23
Ubertini, P., Lebrun, F., Di Cocco, G., et al. 2003, A&A, 411, L131
Ueda, Y., Akayama, M., Ohta, K., & Miyaji, T. 2003, ApJ, 598, 886
Vignali, C., & Comastri, A. 2002, A&A, 381, 834
Vignali, C., Comastri, A., Stirpe, G. M., et al. 1998, A&A, 333, 411
Winkler, C., Courvoisier, T. J.-L., Di Cocco, G., et al. 2003, A&A, 411, L1
Woudt, P. A., Kraan-Korteweg, R. C., Fairall, A. P., et al. 1998, A&A, 338, 8
Young, A. J., Wilson, A. S., Terashima, Y., Arnaud, K. A., & Smith, D. A. 2002, ApJ, 564, 176